MNRAS **000**, 1–18 (2016) Preprint 5th April 2017 Compiled using MNRAS LATEX style file v3.0

Predictions for deep galaxy surveys with *JWST* from ΛCDM

William I. Cowley[1,2]★, Carlton M. Baugh[1], Shaun Cole[1], Carlos S. Frenk[1], Cedric G. Lacey[1]
[1]*Institute for Computational Cosmology, Department of Physics, University of Durham, South Road, Durham, DH1 3LE, UK*
[2]*Kapteyn Astronomical Institute, University of Groningen, PO Box 800, NL-9700 AV Groningen, The Netherlands*

arXiv:1702.02146v2 [astro-ph.GA] 3 Apr 2017

Accepted XXX. Received YYY; in original form ZZZ

ABSTRACT

We present predictions for the outcome of deep galaxy surveys with the *James Webb Space Telescope* (*JWST*) obtained from a physical model of galaxy formation in ΛCDM. We use the latest version of the GALFORM model, embedded within a new $(800\ \mathrm{Mpc})^3$ dark matter only simulation with a halo mass resolution of $M_{\rm halo} > 2 \times 10^9\ h^{-1}\ \mathrm{M}_\odot$. For computing full UV-to-mm galaxy spectral energy distributions, including the absorption and emission of radiation by dust, we use the spectrophotometric radiative transfer code GRASIL. The model is calibrated to reproduce a broad range of observational data at $z \lesssim 6$, and we show here that it can also predict evolution of the rest-frame far-UV luminosity function for $7 \lesssim z \lesssim 10$ which is in good agreement with observations. We make predictions for the evolution of the luminosity function from $z = 16$ to $z = 0$ in all broadband filters on the Near InfraRed Camera (NIRCam) and Mid InfraRed Instrument (MIRI) on *JWST*, and present the resulting galaxy number counts and redshift distributions. Our fiducial model predicts that ~ 1 galaxy per field of view will be observable at $z \sim 10$ for a 10^4 s exposure with NIRCam. A variant model, which produces a higher redshift of reionization in better agreement with *Planck* data, predicts number densities of observable galaxies $\sim 5\times$ greater at this redshift. Similar observations with MIRI are predicted not to detect any galaxies at $z \gtrsim 6$. We also make predictions for the effect of different exposure times on the redshift distributions of galaxies observable with *JWST*, and for the angular sizes of galaxies in *JWST* bands.

Key words: galaxies: formation – galaxies: evolution – galaxies: high-redshift

1 INTRODUCTION

The *James Webb Space Telescope* (*JWST*) is scheduled for launch in October 2018 and is expected to significantly advance our understanding of the high-redshift ($z \gtrsim 7$) Universe (e.g. Gardner et al. 2006). Two of its on-board instruments, the Near InfraRed Camera (NIRCam) and the Mid InfraRed Instrument (MIRI), are dedicated to obtaining broadband photometry over the wavelength range $0.7 - 25.5\ \mu$m with unprecedented sensitivity and angular resolution. This wavelength coverage will enable *JWST* to probe the rest-frame UV/optical/near-IR spectral energy distributions (SEDs) of high-redshift ($z \gtrsim 7$) galaxies, opening up a hitherto unexplored regime of galaxy formation and evolution.

An early breakthrough in the study of galaxies in the high-redshift Universe came from the identification of galaxies at $z \sim 3$ using the Lyman-break technique (e.g. Steidel & Hamilton 1993; Steidel et al. 1996). This study took advantage of the break in galaxy SEDs produced at the Lyman limit (912 Å) to identify galaxies at $z \sim 3$ by searching for 'dropouts' in a set of broadband photometric filters. The significance of this development in the context of galaxy formation and evolution, in particular the implications for the cosmic star formation rate density and the formation of massive galaxies in the ΛCDM cosmological model, was discussed in Baugh et al. (1998, see also Mo & Fukugita 1996 and Mo et al. 1999). A further advance came with the installation of the Advanced Camera for Surveys (ACS) on the *Hubble Space Telescope* which, using the z-band, pushed the Lyman-break technique selection to $z \sim 6$ (e.g. Bouwens et al. 2003; Stanway et al. 2003). At these redshifts the Lyman-break

★ E-mail: cowley@astro.rug.nl (WIC)

© 2016 The Authors

technique makes use of the fact that neutral hydrogen in the intergalactic medium (IGM) effectively absorbs radiation with wavelengths shorter than the Lyman α transition (1216 Å), resulting in a strong break in the galaxy SED at the observer-frame wavelength of this transition. Installation of the Wide-Field Camera 3 (WFC3) with near-IR filters increased the number of galaxies that could be identified at $z \sim 7$ (e.g. Bouwens et al. 2010; Wilkins et al. 2010), pushing the samples of galaxies at these redshifts into the thousands, with a few examples at $z \sim 10$. These advances have been complemented by ground-based telescopes, such as the Visible and Infrared Survey Telescope for Astronomy (VISTA), that typically provide a larger field of view than their space-based counterparts; this has allowed the bright end of the rest-frame far-UV luminosity function to be probed robustly at $z \sim 7$ (e.g. Bowler et al. 2014).

As observations in the near-IR with *Hubble* have identified the highest-redshift galaxies to date, a wealth of further information regarding galaxy properties at intermediate redshifts ($z \sim 3$) has come from surveys with the *Spitzer* Space Telescope in the same wavelength range that will be probed by *JWST* (e.g. Labbé et al. 2005; Caputi et al. 2011, 2015), though *JWST* will have greater angular resolution and sensitivity than *Spitzer*. As a result, *JWST* is expected to greatly increase the number of observed galaxies at $z \gtrsim 7$, providing important information about their SEDs which can help characterise their physical properties, whilst also extending observations of the high-redshift Universe towards the first luminous objects at the end of the so-called cosmic dark ages.

Here we present theoretical predictions for deep galaxy surveys with *JWST* NIRCam and MIRI, in the form of luminosity functions, number counts and redshift distributions from a hierarchical model of galaxy formation within ΛCDM (Lacey et al. 2016). The model provides a physically-motivated computation of galaxy formation from $z \gtrsim 20$ to $z = 0$. For computing galaxy SEDs the model is coupled with the spectrophotometric code GRASIL (Silva et al. 1998), which takes into account the absorption and re-emission of stellar radiation by interstellar dust by solving the equations of radiative transfer in an assumed geometry. The Lacey et al. model is calibrated to reproduce a broad range of observational data at $z \lesssim 6$. A shortcoming of the fiducial Lacey et al. model, however, is that it does not reproduce the reionization redshift of $z = 8.8^{+1.7}_{-1.4}$ inferred from cosmic microwave background (CMB) data by Planck Collaboration et al. (2016). This is an important constraint for high-redshift predictions of the galaxy population. The model produces too few ionizing photons at early times, reionizing the Universe at $z = 6.3$ (Hou et al. 2016).

A simple and effective solution to this shortcoming was proposed by Hou et al. (2016) who, motivated by the dynamical supernova feedback model of Lagos et al. (2013), allowed the strength of supernova feedback in the Lacey et al. (2016) model to vary as a function of redshift. Reducing the strength of supernova feedback at high redshift meant that the model could produce more ionizing photons at this epoch. The evolving feedback also enabled this model to reproduce the $z = 0$ luminosity function of the Milky Way satellites, as well as their metallicity–stellar mass relation. These further successes in matching observational data do not come at the expense of the agreement of the model with the data against which it was originally calibrated at $z \lesssim 6$, but it does introduce new parameters to describe the effects of supernova feedback.

Supernova feedback is an extremely important physical process in galaxy evolution (e.g. Larson 1974; White & Rees 1978; White & Frenk 1991; Cole 1991). However, its precise details, for example, exactly how energy input from supernovae should couple to the interstellar medium (ISM), are still poorly understood. This is mainly due to the difficulty of fully resolving individual star-forming regions in hydrodynamical simulations spanning a cosmologically significant time period and volume (e.g. Vogelsberger et al. 2014; Schaye et al. 2015). It is hoped that comparing the predictions of phenomenological models of supernova feedback, such as those presented here, with future observations from *JWST*, will lead to a greater understanding of this crucial process.

This paper is structured as follows: In Section 2 we present some of the pertinent details of our galaxy formation model and the evolving feedback variant, the radiative transfer code used for the computation of UV-to-mm galaxy SEDs and some information regarding the coupling of these two codes. In Section 3 we present our main results[1]; these include galaxy luminosity functions, number counts and redshift distributions for varying exposures, and angular sizes in each of the NIRCam and MIRI broadband filters. We also present predictions for the evolution of some of the physical properties of the model galaxies (e.g. stellar masses, star formation rates) and compare some model predictions to available high-redshift ($z \gtrsim 7$) observational data. We conclude in Section 4. Throughout we assume a flat ΛCDM cosmology with cosmological parameters consistent with recent *Planck* satellite results (Planck Collaboration et al. 2016)[2]. All magnitudes are presented in the absolute bolometric (AB) system (Oke 1974).

2 THE THEORETICAL MODEL

We now introduce the galaxy formation model, which combines a dark matter only *N*-body simulation, a semi-analytical model of galaxy formation (GALFORM) and the spectrophotometric radiative transfer code GRASIL (Silva et al. 1998) for computing UV-to-mm galaxy SEDs.

2.1 GALFORM

The Durham semi-analytic model of hierarchical galaxy formation, GALFORM, was introduced in Cole et al. (2000), building on ideas outlined earlier by White & Rees (1978), White & Frenk (1991) and Cole et al. (1994). Galaxy formation is modelled *ab initio*, beginning with a specified cosmology and a linear power spectrum of density fluctuations, and ending with predicted galaxy properties at different redshifts.

Galaxies are assumed to form from baryonic condensation within the potential wells of dark matter halos, with

[1] Some of the model data presented here will be made available at http://icc.dur.ac.uk/data/. For other requests please contact the first author.

[2] $\Omega_m = 0.307$, $\Omega_\Lambda = 0.693$, $h = 0.678$, $\Omega_b = 0.0483$, $\sigma_8 = 0.829$

their subsequent evolution being controlled in part by the merging history of the halo. Here, these halo merger trees are extracted directly from a dark matter only N-body simulation (e.g. Helly et al. 2003; Jiang et al. 2014) as this approach allows us to predict directly the spatial distribution of the galaxies. We use a new $(800\ \mathrm{Mpc})^3$ Millennium-style simulation (Springel et al. 2005) with cosmological parameters consistent with recent *Planck* satellite results (Planck Collaboration et al. 2016), henceforth referred to as P–Millennium (Baugh et al. in preparation; McCullagh et al. in preparation). The halo mass resolution of this simulation is $2.12\times10^9\ h^{-1}\ \mathrm{M}_\odot$, where a halo is required to have at least 20 dark matter particles and is defined according to the 'DHalo' algorithm (Jiang et al. 2014). This mass resolution is approximately an order of magnitude better than previous dark matter simulations that were used with this galaxy formation model. For example, the MR7 simulation (Springel et al. 2005; Guo et al. 2013) in which the Lacey et al. (2016) model was originally implemented had a halo mass resolution of $1.87\times10^{10}\ h^{-1}\ \mathrm{M}_\odot$. This improved resolution is particularly important for predictions of the high-redshift Universe where, due to the hierarchical nature of structure formation in ΛCDM, galaxy formation takes place in lower mass halos. This halo mass resolution is in the regime where ignoring baryonic effects on the dark matter, a central assumption of the semi-analytical technique, is still a reasonable one, as the 'back-reaction' due to baryonic effects, such as feedback processes, on the dark matter is expected to reduce the mass of dark matter halos by only ∼ 30 per cent at the mass limit of the P-Millennium simulation (e.g. Sawala et al. 2013).

Baryonic physics in GALFORM are included as a set of coupled differential equations which track the exchange of mass and metals between between the stellar, cold disc gas and hot halo gas components in a given halo. These equations comprise simplified prescriptions for the physical processes (e.g. gas cooling, star formation and feedback) understood to be important for galaxy formation.

Given the change in cosmological parameters, and in the halo mass resolution, from the model presented in Lacey et al. (2016), it is necessary to adjust some of the galaxy formation parameters in the fiducial model such that it can still reproduce certain pre-specified observational datasets to the desired accuracy. These datasets include the optical and near-IR luminosity functions at $z = 0$, the evolution of the rest-frame near-IR luminosity functions for $z = 0-3$, far-IR galaxy number counts and redshift distributions, and the evolution of the rest-frame far-UV luminosity function for $z = 3-6$. The adjustments will be discussed in more detail in Baugh et al. (in preparation); however we briefly summarise the main ideas here. The change in cosmological parameters resulted in a decrease in the physical baryon density, $\Omega_\mathrm{b}h^2$, due to the lower value of the Hubble parameter. This caused the model to produce too few bright galaxies, so the gas reincorporation timescale multiplier, α_ret, was increased to return gas ejected by supernova feedback to the hot halo faster. The change in the halo mass resolution resulted in the number of faint galaxies being overpredicted, so it was necessary to increase the strength of the supernova feedback through increasing the value of the parameter γ_SN, to mitigate this.

Additionally, the model presented here uses an improved prescription for the merger timescale of satellite galaxies from Simha & Cole (2016) that incorporates the effects of both dynamical friction and tidal disruption on a dark matter sub-halo.

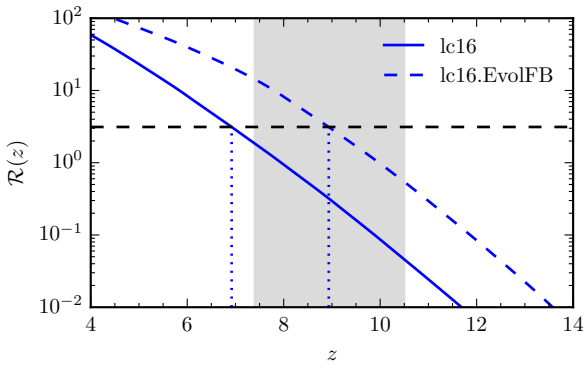

Figure 1. Predicted ratio, $\mathcal{R}(z)$, of the total number of ionizing photons produced before redshift z to the total number of hydrogen nuclei, for the fiducial model (solid blue line) and the evolving feedback variant (dashed blue line). The horizontal black dashed line indicates the ratio at which the IGM is half ionized, $\mathcal{R}_{\mathrm{re,\,half}}$. The grey shaded region indicates the observational estimate of the redshift at which this happens, $z_{\mathrm{re,\,half}} = 8.8^{+1.7}_{-1.4}$, the 68 per cent confidence limit from the *Planck* Collaboration (2016). Dotted vertical lines indicate the values of $z_{\mathrm{re,\,half}}$ predicted by the models.

We summarise these minor adjustments to the model presented in Lacey et al. (2016) in Table 1.

In GALFORM it is assumed that a disc with an exponential profile is formed from cold gas once it has had sufficient time to cool and fall to the centre of the dark matter halo potential well. The size of the disc is solved for by assuming conservation of angular momentum and centrifugal equilibrium (Cole et al. 2000). Galaxy bulges/spheroids are assumed to have a projected $r^{1/4}$ density profile and are formed through a dynamical process, either a disc instability or a galaxy merger. The size of the bulge is determined by the conservation of energy for the components involved i.e. baryons and dark matter in the disc and bulge of the galaxies (Cole et al. 2000). These dynamical processes can also trigger 'bursts' of enhanced star formation. When we refer to starburst galaxies throughout, we are referring to this dynamically triggered star formation rather than, for example, a galaxy's position on the specific star formation rate - stellar mass plane. This distinction is discussed in more detail in Cowley et al. (2016).

2.2 Evolving supernova feedback and the redshift of reionization

As mentioned earlier, a shortcoming of the fiducial Lacey et al. (2016) model is that it does not reionize the Universe at a redshift as high as implied by recent *Planck* data, as it does not produce enough ionizing photons at early enough times. Here we discuss the variant feedback model of Hou et al. (2016) which provides a simple and effective solution to this shortcoming.

In the fiducial GALFORM model supernova feedback is implemented such that energy input into the interstellar me-

Table 1. Changes between parameter values presented in Lacey et al. (2016) and those used in this work (and discussed further in Baugh et al. in preparation). The galaxy formation parameters are listed in the bottom part of the table.

Parameter	Description	Lacey et al. (2016)	This work
Cosmological parameters		Komatsu et al. (2011)	*Planck* Collaboration (2016)
Ω_m	Matter density	0.272	0.307
Ω_Λ	Vacuum energy density	0.728	0.693
Ω_b	Baryon density	0.0455	0.0483
h	Hubble Parameter	0.704	0.678
σ_8	Fluctuation amplitude	0.810	0.829
N-body simulation parameters			
$M_\mathrm{halo,min}$	Minimum halo mass	$1.87 \times 10^{10}\ h^{-1}\ \mathrm{M}_\odot$	$2.12 \times 10^{9}\ h^{-1}\ \mathrm{M}_\odot$
Galaxy merger timescale		Jiang et al. (2008)	Simha & Cole (2016)
Galaxy formation parameters			
α_ret	Gas reincorporation timescale multiplier	0.64	1.0
γ_SN	Slope of SN feedback mass loading	3.2	3.4

dium (ISM) by supernovae causes gas to be ejected out of the disc. It is parametrised as

$$\dot{M}_\mathrm{eject} = \beta(V_\mathrm{c})\psi = (V_\mathrm{c}/V_\mathrm{SN})^{-\gamma_\mathrm{SN}}\psi. \quad (1)$$

Here $\dot{M}_\mathrm{eject}$ is the rate at which cold disc gas is ejected beyond the virial radius of the halo[3]; β is the mass loading factor; V_c is the circular velocity of the disc; ψ is the star formation rate; and V_SN and γ_SN are adjustable parameters. We assume $V_\mathrm{SN} = 320$ km s^{-1} (Lacey et al. 2016) and $\gamma_\mathrm{SN} = 3.4$ (Baugh et al. in preparation).

In order to produce more ionizing photons, and thus reionize the Universe earlier than the fiducial model, Hou et al., motivated by the dynamical supernova feedback model of Lagos et al. (2013), introduced a break into the power-law parametrisation of the mass loading factor and also a redshift dependence into its normalisation, such that

$$\beta(V_\mathrm{c}, z) = \begin{cases} [V_\mathrm{c}/V'_\mathrm{SN}(z)]^{-\gamma'_\mathrm{SN}} & V_\mathrm{c} \le V_\mathrm{thresh} \\ [V_\mathrm{c}/V_\mathrm{SN}(z)]^{-\gamma_\mathrm{SN}} & V_\mathrm{c} > V_\mathrm{thresh}, \end{cases} \quad (2)$$

where V_thresh and γ'_SN are additional adjustable parameters [$V'_\mathrm{SN}(z)$ is set by the condition that β be a continuous function at $V_\mathrm{c} = V_\mathrm{thresh}$]. The redshift evolution of the normalisation is parametrised as

$$V_\mathrm{SN}(z) = \begin{cases} V_\mathrm{SN2} & z > z_\mathrm{SN2} \\ c_0\, z + c_1 & z_\mathrm{SN2} \le z \le z_\mathrm{SN1} \\ V_\mathrm{SN1} & z < z_\mathrm{SN1}, \end{cases} \quad (3)$$

where V_SN2, z_SN2 and z_SN1 are additional adjustable parameters [the constants c_0 and c_1 are set by the condition that $V_\mathrm{SN}(z)$ be a continuous function]. Here we use the same values for these additional adjustable parameters as Hou et al.: $V_\mathrm{thresh} = 50$ km s^{-1}, $\gamma'_\mathrm{SN} = 1.0$, $V_\mathrm{SN2} = 180$ km s^{-1}, $z_\mathrm{SN1} = 4$ and $z_\mathrm{SN2} = 8$, without any further calibration, although we remind the reader that the value for γ_SN is different to the one used by Hou et al. Additionally, we adopt $V_\mathrm{SN1} = V_\mathrm{SN}$, as was done by Hou et al.

We show the predicted redshift of reionization for both the fiducial model (lc16) and the evolving feedback variant (lc16.EvolFB) in Fig. 1. Following Hou et al. we calculate the ratio, $\mathcal{R}(z)$, of ionizing photons produced before redshift z, to the number density of hydrogen nuclei as

$$\mathcal{R}(z) = \frac{\int_z^\infty \epsilon(z')\,\mathrm{d}z'}{n_\mathrm{H}}, \quad (4)$$

where $\epsilon(z')$ is the number of hydrogen-ionizing photons produced per unit comoving volume per unit redshift at redshift z' and n_H is the comoving number density of hydrogen nuclei. The Universe is assumed to be fully ionized at redshift $z_\mathrm{re,full}$, for which,

$$\mathcal{R}(z_\mathrm{re,full}) = \frac{1 + N_\mathrm{rec}}{f_\mathrm{esc}}, \quad (5)$$

where N_rec is the mean number of recombinations per hydrogen atom up to reionization, and f_esc is the fraction of ionizing photons that can escape into the IGM from the galaxy producing them. Here we adopt $N_\mathrm{rec} = 0.25$ and $f_\mathrm{esc} = 0.2$ as was done by Hou et al. This gives a threshold for reionization of $\mathcal{R}(z_\mathrm{re,full}) = 6.25$.

Observations of the CMB (e.g. Planck Collaboration et al. 2016) directly constrain the electron scattering optical depth to recombination, which is then converted to a reionization redshift by assuming a simple model for the redshift dependence of reionization (e.g. Appendix B of Lewis et al., 2008). The redshift of reionization is commonly expressed in terms of the redshift, $z_\mathrm{re,half}$, at which half of the IGM is reionized. Here we assume $\mathcal{R}_\mathrm{re,half} = 0.5\,\mathcal{R}_\mathrm{re,full}$ as was done by Hou et al. The value of $\mathcal{R}_\mathrm{re,half}$ is shown as the horizontal dashed line in Fig. 1. We can see that the evolving feedback model predicts $z_\mathrm{re,half} = 8.9$, in good agreement with the 68 per cent confidence interval inferred from *Planck* satellite data (Planck Collaboration et al. 2016), $z_\mathrm{re,half} = 8.8^{+1.7}_{-1.4}$. For the fiducial model the reionization redshift turns out to be lower, $z_\mathrm{re,half} = 6.9$, which is discrepant by $\sim 1.5\sigma$ with the *Planck* data.

2.3 The Dust Model

We use the spectrophotometric radiative transfer code GRASIL (Silva et al. 1998) to compute model galaxy SEDs. Using the star formation and metal enrichment histories, gas masses and geometrical parameters predicted by GALFORM, and assuming a composition and geometry for interstellar dust, GRASIL computes the SEDs of the model galaxies, accounting for dust extinction (absorption and scattering) of radiation and its subsequent re-emission. In this Section we

[3] This gas eventually falls back within the virial radius on a timescale which depends on the dynamical time of the halo (see Lacey et al. 2016).

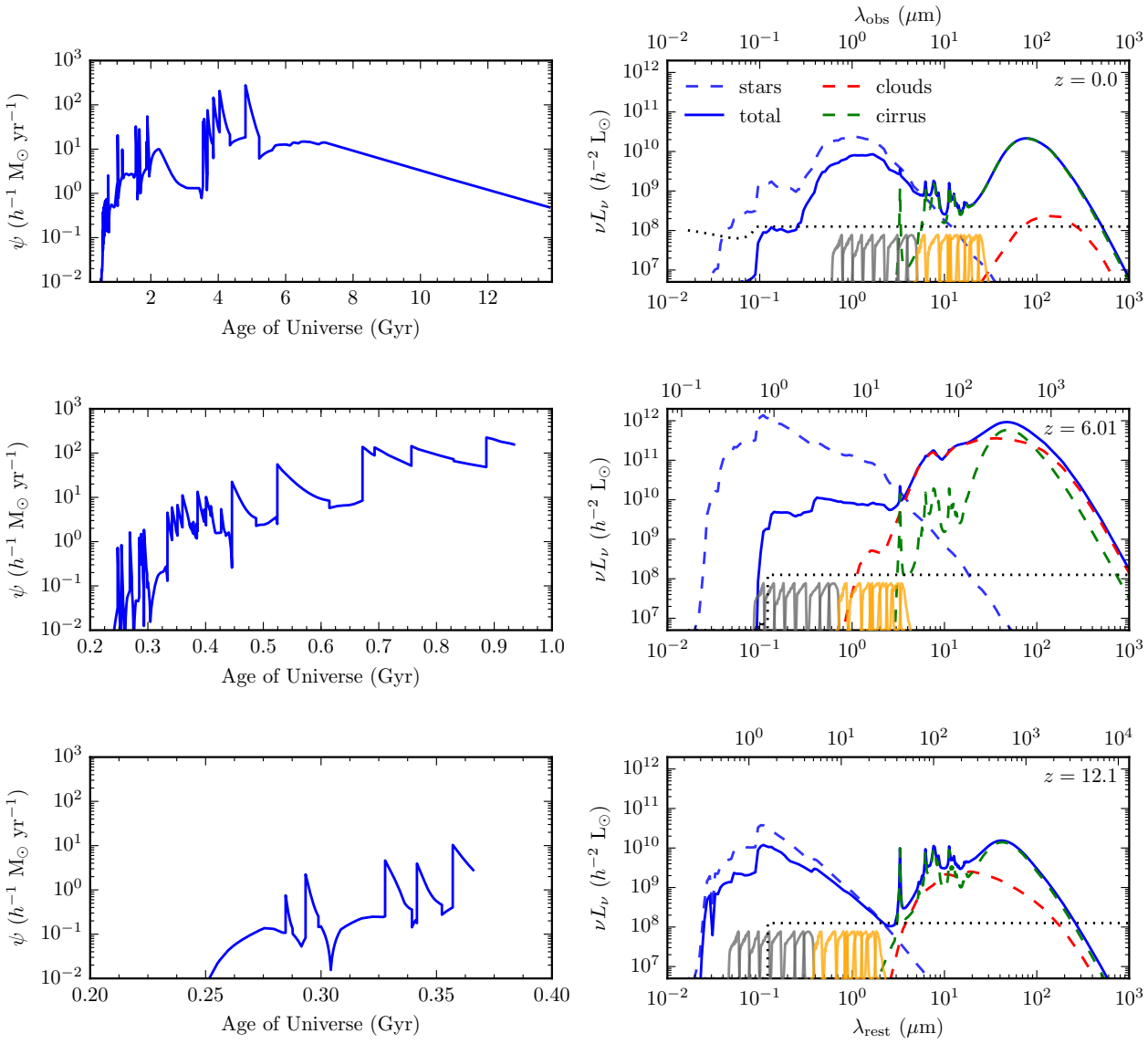

Figure 2. Example galaxy star formation histories and SEDs. Each row shows a galaxy selected at a different redshift, as indicated in the right panels. *Left panels*: star formation histories of three galaxies (in each case summed over all of the galaxy's progenitors) predicted by GALFORM. Note that the range of the abscissa is different in each panel. *Right panels*: corresponding galaxy SEDs predicted by GRASIL (Silva et al. 1998), plotted against rest-frame wavelength on the bottom axis and observed wavelength on the top axis. The dashed blue line is the intrinsic stellar SED. The solid blue line is the total galaxy SED including dust absorption and emission. The dashed red and green lines are the dust emission for the molecular cloud and diffuse cirrus components respectively. The *JWST* filter transmission functions for NIRCam (MIRI) bands are shown in grey (orange), in arbitrary units. The intergalactic medium (IGM) transmission function of Meiksin (2005) is shown by the dotted black line (also in arbitrary units).

briefly describe the GRASIL model. For further details we refer the reader to Silva et al. (1998) and Granato et al. (2000).

Here GRASIL assumes that stars exists in a disc + bulge system, as is the case in GALFORM. The disc has a radial and vertical exponential profile with scale lengths, h_R and h_z, and the bulge is described by an analytic King model profile, $\rho \propto (r^2 + r_{\rm c}^2)^{-3/2}$ out to a truncation radius, $r_{\rm t}$. The half-mass radii, $r_{\rm disc}$ and $r_{\rm bulge}$, are predicted by GALFORM. By definition, given the assumed profiles, the bulge core radius is related to the half-mass radius by $r_{\rm c} = r_{\rm bulge}/14.6$ whilst the radial disc scale-length, $h_{\rm R}$, is related to the half-mass disc radius by $h_R = r_{\rm disc}/1.68$. Star formation histories are calculated separately for the disc and bulge by GALFORM. For galaxies undergoing a starburst, the burst star formation, as well as the associated gas and dust, are assumed to also be in an exponential disc but with a half-mass radius, $r_{\rm burst} = \eta r_{\rm bulge}$, rather than $r_{\rm disc}$, where η is an adjustable parameter. The disc axial ratio, h_z/h_R, is a parameter of the GRASIL model; for starburst galaxies the axial ratio of the burst is allowed to be different from that of discs in quiescent galaxies.

The gas and dust exist in an exponential disc, with the same radial scale-length as the disc stars but in general with

Table 2. Adopted values for adjustable parameters in GRASIL. See the text in Section 2.3 for their definitions.

Parameter	Value
h_z/h_R (disc)	0.1
h_z/h_R (burst)	0.5
h_z(dust)/h_z(stars)	1
η	1.0
$f_{\rm cloud}$	0.5
$m_{\rm cloud}/r^2_{\rm cloud}$	10^6 M$_\odot$/(16 pc)^2
$t_{\rm esc}$	1 Myr
$\beta_{\rm b}$	1.5

a different scale-height, so h_z(dust)/h_z(stars) is an adjustable parameter. The gas and dust are assumed to exist in two components: (i) giant molecular clouds in which stars form, escaping on some time scale, $t_{\rm esc}$, and (ii) a diffuse cirrus ISM. The total gas mass, $M_{\rm cold}$, and metallicity, $Z_{\rm cold}$, are calculated by GALFORM. The fraction of gas in molecular clouds is determined by the parameter $f_{\rm cloud}$. The cloud mass, $m_{\rm cloud}$, and radius, $r_{\rm cloud}$, are also parameters, though the results of the model depend only on the ratio, $m_{\rm cloud}/r^2_{\rm cloud}$, which determines (together with the gas metallicity) the optical depth of the clouds.

The dust is assumed to consist of a mixture of graphite and silicate grains and polycyclic aromatic hydrocarbons (PAHs), each with a distribution of grain sizes. The grain mix and size distribution were determined by Silva et al. so that the extinction and emissivity properties of the local ISM are reproduced using the optical properties of the dust grains tabulated by Draine & Lee (1984). At long wavelengths ($\lambda > 30$ μm) this results in a dust opacity that approximates $\kappa_{\rm d} \propto \lambda^{-2}$. However, in galaxies undergoing a starburst this is modified (for $\lambda > 100$ μm) such that $\kappa_{\rm d} \propto \lambda^{-\beta_{\rm b}}$, where $\beta_{\rm b}$ is treated as an adjustable parameter. Laboratory measurements suggest that values in the range $\beta_{\rm b} = 1.5 - 2$ are acceptable (Agladze et al. 1996). Here a value of $\beta_{\rm b} = 1.5$ is adopted (Lacey et al. 2016). The total dust mass in a galaxy is proportional to the cold gas mass and metallicity, which are predicted by GALFORM.

The adopted values of adjustable GRASIL parameters are summarised in Table 2. For the parameters which are analogous to those in the dust model used by Lacey et al. (2016): $f_{\rm cloud}$, $m_{\rm cloud}/r^2_{\rm cloud}$, $t_{\rm esc}$ and $\beta_{\rm b}$, we use the values chosen by Lacey et al. For other parameters specific to the GRASIL model, we use the values chosen by by Baugh et al. (2005, see also Lacey et al. 2008, Swinbank et al. 2008 and Lacey et al. 2011), which was the last time a published version of GALFORM was coupled with GRASIL in the manner presented here.

The luminosities of the stellar components are calculated assuming the Maraston (2005) evolutionary population synthesis model, as is done in Lacey et al. (2016). GRASIL then calculates the radiative transfer of the stellar radiation through the interstellar dust. For molecular clouds a full radiative transfer calculation is performed. For the diffuse cirrus the effects of scattering are included approximately by using an effective optical depth for the absorption $\tau_{\rm abs,eff} = [\tau_{\rm abs}(\tau_{\rm abs} + \tau_{\rm scat})]^{1/2}$. The dust-attenuated stellar radiation field can be calculated at any point inside or outside the galaxy. GRASIL then computes the final galaxy SED by calculating the absorption of stellar radiation, thermal balance and the re-emission of radiation for each grain species and size at every point in the galaxy.

Examples of predicted star formation histories and the resulting galaxy UV-to-mm SEDs computed by GRASIL are shown in Fig. 2. One can see that the star formation histories are extremely 'bursty' at early times, when the Universe is a few Gyr old. Significant dust extinction and re-emission is evident for each of the galaxy SEDs shown. There are also a number of interesting features in the galaxy SEDs. These include: (i) Lyman-continuum breaks in the galaxy SEDs at 912 Å; (ii) a prominent 4000 Å break for the $z = 0$ galaxy, indicative of an old stellar population (which would be expected from the smoothly declining star formation history of this galaxy); (iii) dust emission approximating a modified blackbody that peaks at $\lambda_{\rm rest} \approx 100$ μm, indicative of cold (~ 30 K) dust, though the peak of the emission shifts to shorter wavelengths with increasing redshift suggesting hotter dust, and (iv) PAH emission lines in the cirrus dust at $\lambda_{\rm rest} = 3.3$, 6.2, 7.7, 8.6, and 11.3 μm.

Once an SED has been computed, luminosities in specified bands are calculated by convolving the SED (redshifted into the observer frame) with the filter transmission of interest. We use the Meiksin (2005) prescription for attenuation of radiation in the intergalactic medium (IGM) due to neutral hydrogen, also shown in Fig. 2.

2.4 Coupling GALFORM and GRASIL

Here we briefly describe how the GALFORM and GRASIL models are used in conjunction. For further details we refer the reader to Granato et al. (2000).

Due to the computational expense of running GRASIL ($\sim 3-5$ CPU mins per galaxy) it is not feasible to compute an SED for each galaxy in the simulation volume, as has been discussed in previous studies (e.g. Granato et al. 2000; Almeida et al. 2010; Lacey et al. 2011). However, for the purposes of constructing luminosity functions it is possible to circumvent this by running GRASIL on a sample of galaxies, from which the luminosity function can be constructed if the galaxies in question are weighted appropriately. We choose to sample galaxies according to their stellar mass such that $\sim 10^3$ galaxies per dex of stellar mass are sampled. We use a lower mass limit of 10^6 h^{-1} M$_\odot$, which we choose so that any artificial features it introduces into our predicted luminosity functions (see Section 3.2) are at fainter luminosities than are investigated here. This represents a factor of ~ 10 increase over the number of galaxies sampled by Granato et al. (2000).

The procedure that we use to construct luminosity functions in a given band at each output redshift is as follows: (i) run GALFORM to the redshift of interest; (ii) create a subsample of galaxies; (iii) re-run GALFORM to output the star formation and metal enrichment history for each of the sampled galaxies; (iv) run GRASIL on each of the sampled galaxies to produce a predicted SED; (v) convolve the output SED with the relevant broadband filter response and IGM attenuation curve (Meiksin 2005) and (vi) construct the galaxy luminosity function using the weights from the initial sampling and luminosities from the previous step.

We have made a number of improvements to steps (iii) to (v) above, which allow us to run GRASIL for samples of $\sim 10^5$ galaxies for each model, spread over 25 output redshifts

from $z = 16$ to $z = 0$. For each model, this takes $\sim 7 \times 10^3$ CPU hours, approximately 95 per cent of which is spent by GRASIL, with the remaining time being taken by GALFORM to calculate the necessary star formation histories.

3 RESULTS

In this Section we present our main results. In Section 3.1 we present predictions for the evolution of physical properties of the galaxy population as well as a comparison of our predictions with available high-redshift ($z \gtrsim 7$) observational data. In Section 3.2 we present the predicted evolution of the galaxy luminosity function for the NIRCam–F200W and MIRI–F560W filters. We make such predictions for each NIRCam and MIRI broadband filter but only show these two in this paper for brevity; results for other filters will be made available online. In Section 3.3 we present predictions for galaxy number counts and redshift distributions (for a 10^4 s exposure) observable by *JWST* in each NIRCam and MIRI band; we also show predictions for the redshift distributions of galaxies observable with longer (10^5 and 10^6 s) exposures. Finally, in Section 3.4 we present predictions for the angular sizes of galaxies for the NIRCam–F200W and MIRI–F560W filters, again we make such predictions for all NIRCam filters but show only these two here for brevity. Throughout we show predictions for our fiducial model 'lc16' and the variant 'lc16.EvolFB' that adopts the evolving feedback model presented in Hou et al. (2016) and is discussed in Section 2.2.

3.1 The Lacey et al. (2016) model at high redshift

In this Section we present model predictions for the evolution of the physical properties of the galaxy population and compare our predictions at $z \gtrsim 7$ to available observational data. In Fig. 3 we show predictions of the fiducial and evolving feedback variant models for the evolution of: (a) the galaxy stellar mass function; (b) the galaxy star formation rate function (for $M_\star > 10^6\ h^{-1}\ \mathrm{M}_\odot$ galaxies); and (c) the fraction of bulge-dominated (i.e. with bulge-to-total stellar mass ratios of $B/T > 0.5$) galaxies as a function of stellar mass, from $z = 15.1$ to $z = 0$.

The stellar mass function [Fig. 3 (a)] evolves strongly until $z \sim 2$ for both models. At lower redshifts further evolution is predominantly at the high-mass end. It is easily seen that (for $z \gtrsim 2$) the evolving feedback model results in both more massive galaxies and a greater abundance of galaxies at a given stellar mass (for $M_\star \gtrsim 10^6\ h^{-1}\ \mathrm{M}_\odot$, as galaxies with a lower stellar mass are not included in our GRASIL sampling) by factors of up to ~ 10. For $z < 4$, the normalisation of the supernova feedback strength is the same in both models and the differences between their stellar mass functions begin to disappear. At the low mass end ($M_\star \lesssim 10^8\ h^{-1}\ \mathrm{M}_\odot$), however, the break in the power law for the mass-loading factor (at $V_\mathrm{thresh} = 50$ km s^{-1}) in the evolving feedback model results in a greater abundance of galaxies at these stellar masses than in the fiducial model. At the high mass end ($M_\star \gtrsim 10^{11}$), an increase in stellar mass at low redshift due to the reduced feedback strength at higher redshift is apparent.

The distribution of star formation rates [Fig. 3 (b)] tells a similar story. For $z < 4$ the distributions predicted by both models are essentially identical, except at low star formation rates (SFRs $\lesssim 10^{-2}\ h^{-1}\ \mathrm{M}_\odot\ \mathrm{yr}^{-1}$) where the break in the evolving feedback model results in this model having a greater abundance of galaxies. At higher redshifts $z > 4$ the differences in the star formation rate distributions are greater due to the different normalisations of feedback, with the evolving feedback variant having significantly more galaxies with SFRs $\gtrsim 3{\times}10^{-2}\ h^{-1}\ \mathrm{M}_\odot\ \mathrm{yr}^{-1}$. The apparent peak seen in each SFR distribution is mostly due to the imposed stellar mass limit of $10^6\ h^{-1}\ \mathrm{M}_\odot$, if lower stellar mass galaxies were included it would shift to lower star formation rates according to the (approximately) constant relation between specific star formation rate and stellar mass predicted by the model (e.g. Mitchell et al. 2014; Cowley et al. 2016).

Fig. 3 (c) shows the evolution in the fraction of galaxies with a bulge-to-total stellar mass ratio of $B/T > 0.5$, as a function of total stellar mass. In GALFORM, bulges are created by a dynamical process, either a galaxy merger or a disc instability. The transition from a disc-dominated to a bulge-dominated galaxy population is relatively sharp, occurring over roughly one dex in stellar mass in most cases. In the evolving feedback model this transition generally occurs at lower stellar masses. At higher redshifts (and thus lower stellar masses), the shape of the relation is different for the evolving feedback variant, which predicts a much smoother transition. We caution against over interpreting the predicted B/T as a proxy for morphological type. The instabilities that create bulges in GALFORM do not necessarily create slowly rotating bulges, and so defining bulges as slow rotators would give different results to those presented here.

Having established some predicted physical properties of galaxies in the two models, we now compare predictions of the models to observational data at $z \gtrsim 7$. We note that none of the observational data considered here were used to calibrate model parameters [Lacey et al. (2016) only considered rest-frame far-UV luminosity functions at $z \lesssim 6$ in their model calibration].

We compare the predictions of the models for the evolution of the rest-frame far-UV luminosity function to observational data over the redshift interval $7 \lesssim z \lesssim 10$ in Fig. 4. We can see that both models provide reasonable agreement with the observed data, and appear to 'bracket' the data for $M_\mathrm{AB}(1500\ \text{Å}) - 5\log_{10} h \gtrsim -18$. However, at brighter magnitudes the predictions of the two models converge. This is due to dust extinction becoming the limiting factor in a galaxy's intrinsic brightness at far-UV wavelengths. To illustrate this, we show the predictions of the two models, without dust attenuation, in the $z = 10$ panel. These predictions resemble the star formation rate distributions in Fig. 3 (b), as the star formation rate of a galaxy is essentially traced by the rest-frame far-UV.

Finally, we compare predictions for the angular sizes of galaxies to observational data in the redshift range $7 \lesssim z \lesssim 9$ in Fig 5. The stellar component of the model galaxies is assumed to be a composite system, consisting of an exponential disc and a bulge with a projected $r^{1/4}$ density profile (Cole et al. 2000). We compute the half-light radii for our model galaxies by weighting the density profile of each component by their predicted rest-frame far-UV (1500 Å) luminosity, dividing the half-light radii of the disc by a factor of 1.34 to account for inclination effects (Lacey et al. 2016),

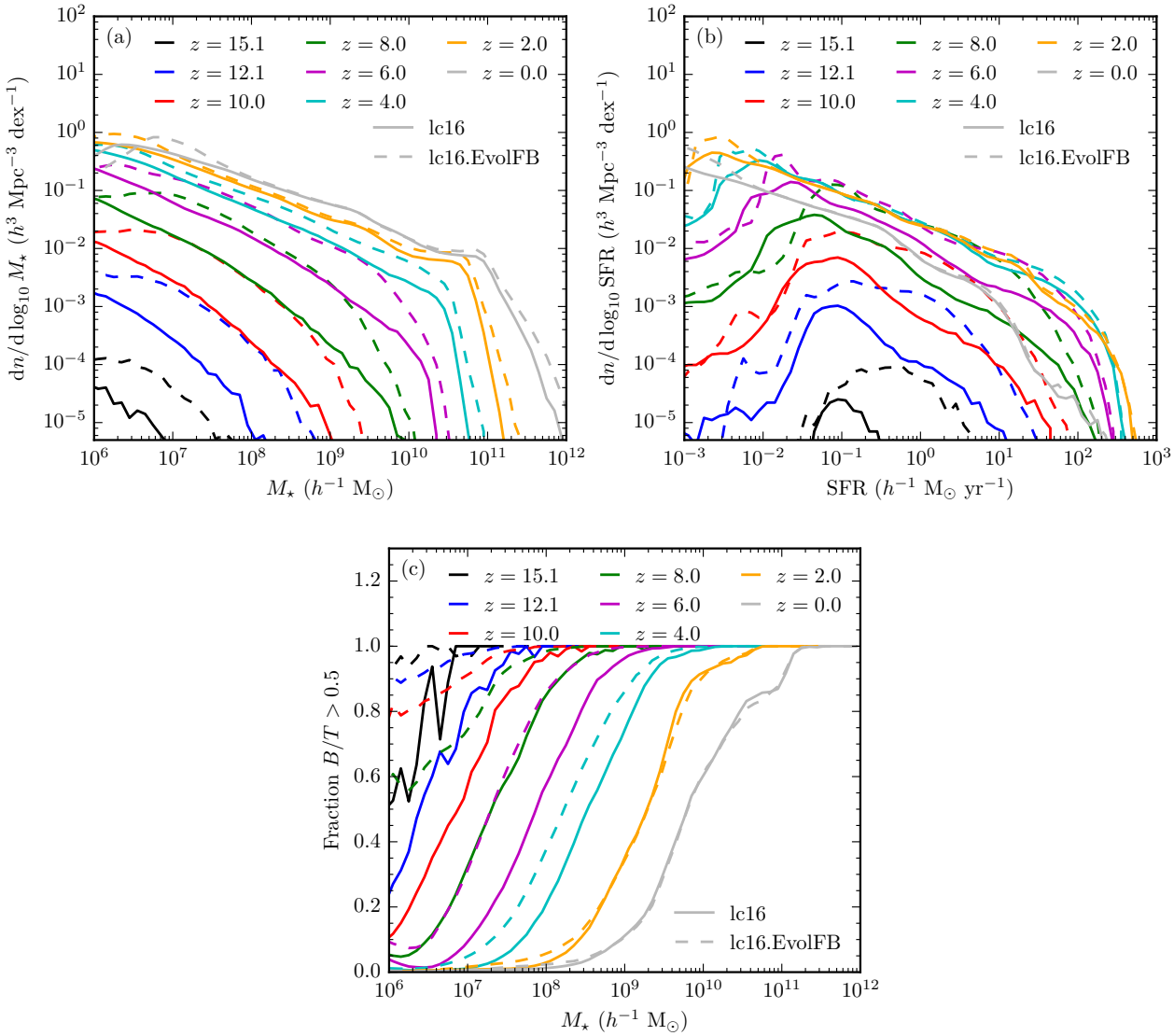

Figure 3. Predicted evolution of physical galaxy properties from $z = 15.1$ to $z = 0$. *Panel (a)*: the galaxy stellar mass function. *Panel (b)*: the star formation rate function for galaxies with $M_\star > 10^6\ h^{-1}\ \mathrm{M}_\odot$. *Panel (c)*: the fraction of bulge-dominated (bulge-to-total stellar mass ratios, $B/T > 0.5$) galaxies as a function of stellar mass. In each panel the colour of the line indicates the redshift as shown in the legend. The solid lines are predictions from the fiducial model whereas the dashed lines are predictions from the evolving feedback variant.

and interpolating to find the half-light radius of the composite system. We then bin the galaxies according to their flux, S_ν. The symbols in Fig. 5 show the median size in each flux bin, with the errorbars representing the 16 – 84 percentile scatter in each bin. We show this for the whole galaxy population, and also split into starburst and quiescent galaxies. The differences between the predictions of the two models are small and they both show reasonable agreement with data from Ono et al. (2013) and Shibuya et al. (2015), who use GALFIT (Peng et al. 2002) to derive sizes from *Hubble Space Telescope* imaging. For the Ono et al. data we present their stacked image results. For the Shibuya et al. data we bin their sizes for individual galaxies into bins of 1 mag width and present the median size in each bin. The errorbars presented represent the 16−84 percentile scatter of sizes within these bins. For reference, we also show the diffraction limit of *JWST*. The models predict that *JWST* should be able to resolve most galaxies in the rest-frame far-UV at these redshifts.

In summary, the predictions of both models show good agreement with the evolution of the rest-frame far-UV (1500 Å) luminosity function and observed galaxy sizes at high redshift ($z \gtrsim 7$). We re-iterate that these high-redshift data were not considered when calibrating the model.

3.2 Luminosity functions observable with *JWST*

In this Section we present predictions for the evolution of the galaxy luminosity function in the *JWST* NIRCam and MIRI bands. These are listed in Table 3, with their sens-

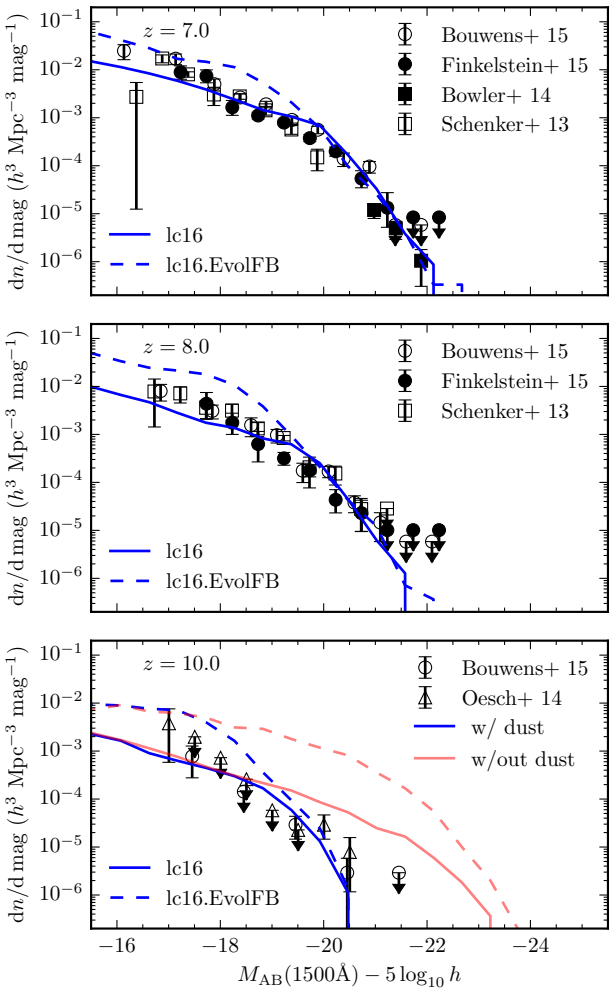

Figure 4. The predicted rest-frame far-UV (1500 Å) luminosity functions for $z = 7 - 10$ for the fiducial model (solid blue line) and the evolving feedback variant (dashed blue line). The redshift is indicated in each panel. Observational data are from Bouwens et al. (2015, open circles), Finkelstein et al. (2015, filled circles), Bowler et al. (2014, filled squares), Schenker et al. (2013, open squares) and Oesch et al. (2014, open triangles) as indicated in the legend. In the bottom panel the red lines show the model predictions without dust extinction.

itivities (for a 10^4 s exposure), and the field of view (FoV) for each instrument is shown in Table 4. In Fig. 6 we show the predicted luminosity functions for the NIRCam–F200W and MIRI–F560W bands. We make such predictions for all broadband NIRCam and MIRI filters, but show only these two here for brevity. The predictions for other filters will be made available online.

In the top panels of Fig. 6 we can see that at high redshifts the difference between the two models is similar to that seen in Fig. 4, and that the models predict similar luminosity functions for $z < 4$, when the normalisation of the feedback strength is the same in both models.

In the bottom panels we show the predicted luminosity function at $z = 10$ for NIRCam–F200W (bottom left panel), and at $z = 6$ for MIRI–F560W (bottom right panel). We choose these values as they are the redshifts at which we predict *JWST* will see ~ 1 object per field of view (FoV) for a 10^4 s exposure, as is discussed below. Here we show the contribution to the luminosity function predicted by the fiducial model from quiescent and starburst galaxies. We can see that the bright end of the luminosity function is dominated by galaxies undergoing a burst of star formation. As mentioned earlier, the definition of starburst here refers to a dynamical process, either a galaxy merger or disc instability, triggering a period of enhanced star formation. We also show predictions of the fiducial model without dust, and can see that the bright end of the luminosity functions at these redshifts is composed of heavily dust-attenuated objects. We therefore expect such observations to provide a further constraint on the way dust absorption is accounted for in galaxy formation models.

For reference we have also shown the sensitivity limits of the filters based on 10^4 and 10^5 s exposures as the vertical dashed and dotted lines respectively. Our adopted sensitivities for a 10^4 s exposure are summarised in Table 3. We derive sensitivities for other exposures assuming they scale as $t^{-1/2}$.

In conjunction we also show the abundance at which the instrument will see one object per FoV per unit redshift at this redshift. Our adopted fields of view are summarised in

Table 3. Adopted sensitivities for *JWST* filters based on 10σ point source and 10^4 s exposure.

Instrument	Filter	λ_{eff} (μm)	Sensitivity (μJy)
NIRCam	F070W	0.70	20.9×10^{-3}
	F090W	0.90	14.3×10^{-3}
	F115W	1.15	11.8×10^{-3}
	F150W	1.50	11.2×10^{-3}
	F200W	2.00	11.4×10^{-3}
	F277W	2.77	12.3×10^{-3}
	F356W	3.56	13.8×10^{-3}
	F444W	4.44	24.5×10^{-3}
MIRI	F560W	5.6	0.2
	F770W	7.7	0.28
	F1000W	10.0	0.7
	F1130W	11.3	1.7
	F1280W	12.8	1.4
	F1500W	15.0	1.8
	F1800W	18.0	4.3
	F2100W	21.0	8.6
	F2550W	25.5	28

Note: Adapted from http://www.stsci.edu/jwst/instruments/nircam/sensitivity/table (NIRCam) and http://www.stsci.edu/jwst/instruments/miri/docarchive/miri-pocket-guide.pdf (MIRI).

Table 4. Adopted *JWST* instrument fields of view (FoV).

Instrument	FoV (arcmin^2)
NIRCam	2.2×2.2
MIRI	1.25×1.88

Note: From http://www.stsci.edu/jwst/instruments/nircam/nircam-glance (NIRCam) and http://www.stsci.edu/jwst/instruments/miri/miri-glance (MIRI).

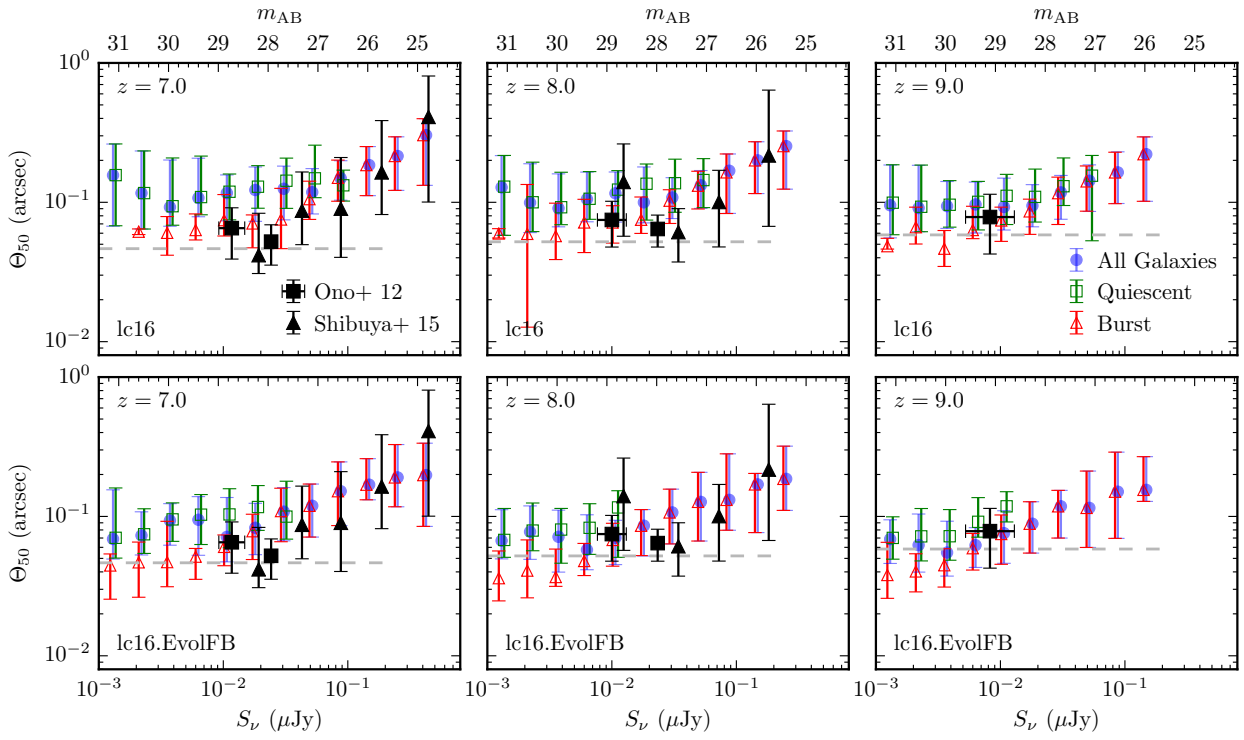

Figure 5. Predicted rest-frame far-UV (1500 Å) galaxy projected half-light radii for $z = 7 - 9$, as a function of galaxy flux, S_ν. The redshift is indicated in each panel. The top row shows predictions from the fiducial model, whereas the bottom row shows predictions from the evolving feedback variant. Blue filled circles indicate the median size for all galaxies at a given flux, with the errorbars indicating the 16 – 84 percentile range. The open green squares and red triangles indicate this for quiescent and starburst galaxies respectively. Observational data are from Ono et al. (2013, black filled squares) and Shibuya et al. (2015, black filled triangles). For reference, the horizontal dashed line in each panel indicates the diffraction limit for *JWST* for a fixed rest-frame wavelength of 1500 Å, assuming a 6.5 m diameter mirror.

Table 4. Objects that are in the upper right quadrant of each plot would be observable with a 10^4 s exposure in a single FoV. Therefore, the fiducial model predicts that ~ 1 object will be observable at $z = 10$ by NIRCam–F200W, and ~ 2 will be observable at $z = 6$ by MIRI–F560W. We recognise that single FoV observations will be sensitive to field-to-field variance. We hope to make direct predictions for the field-to-field variance by creating lightcone catalogues from our simulation in a future work.

3.3 Galaxy number counts and redshift distributions observable with *JWST*

The simplest statistic of a galaxy population that can be derived from an imaging survey is their number counts. Here we present the predictions for the cumulative number counts observable with NIRCam (Fig. 7) and MIRI (Fig. 8). We also show the corresponding redshift distributions (for a 10^4 s exposure) in Fig. 9 (NIRCam) and Fig. 10 (MIRI). We obtain the number counts and redshift distributions by integrating the predicted luminosity functions according to

$$\frac{\mathrm{d}^3\eta}{\mathrm{d}\ln S_\nu\,\mathrm{d}z\,\mathrm{d}\Omega} = \frac{\mathrm{d}n}{\mathrm{d}\ln L_\nu}\frac{\mathrm{d}^2V}{\mathrm{d}z\,\mathrm{d}\Omega}, \tag{6}$$

where η is the surface density of galaxies projected on the sky, n is the number density of galaxies and $\mathrm{d}^2V/\mathrm{d}z\,\mathrm{d}\Omega$ is the comoving volume element per unit solid angle. We show the contribution to the predicted number counts and redshift distributions from quiescent and starburst galaxies. For the NIRCam filters the counts are dominated by quiescent galaxies. This is because they are dominated by galaxies at low redshift, for which starbursts are not a significant population at these wavelengths. This is also why the predicted number counts from the fiducial and evolving feedback variant models are so similar, as at low redshifts the feedback normalisations are equal, though the lc16.EvolFB model does predict slightly more galaxies at faint fluxes. For the MIRI number counts we see the burst population becoming important at brighter fluxes in bands $\lambda_{\rm obs} \gtrsim 10$ μm. These wavelengths also correspond to a shift from the number counts being dominated by dust-attenuated stellar light to dust emission. Again, these number counts are dominated by relatively low-redshift galaxies, for which the MIRI filters probe the dust emission from the rest-frame mid-IR.

The redshift distributions in Figs 9 and 10 exhibit a more discernible difference between the two models, particularly in the NIRCam bands at high redshift. For instance, in the NIRCam–F200W filter, the redshift at which one object per FoV per unit redshift is observable with a 10^4 s exposure is $z \sim 10$. For the evolving feedback variant ~ 5 times more galaxies are predicted to be observable at this redshift. From our predictions it appears that very few galaxies will be ob-

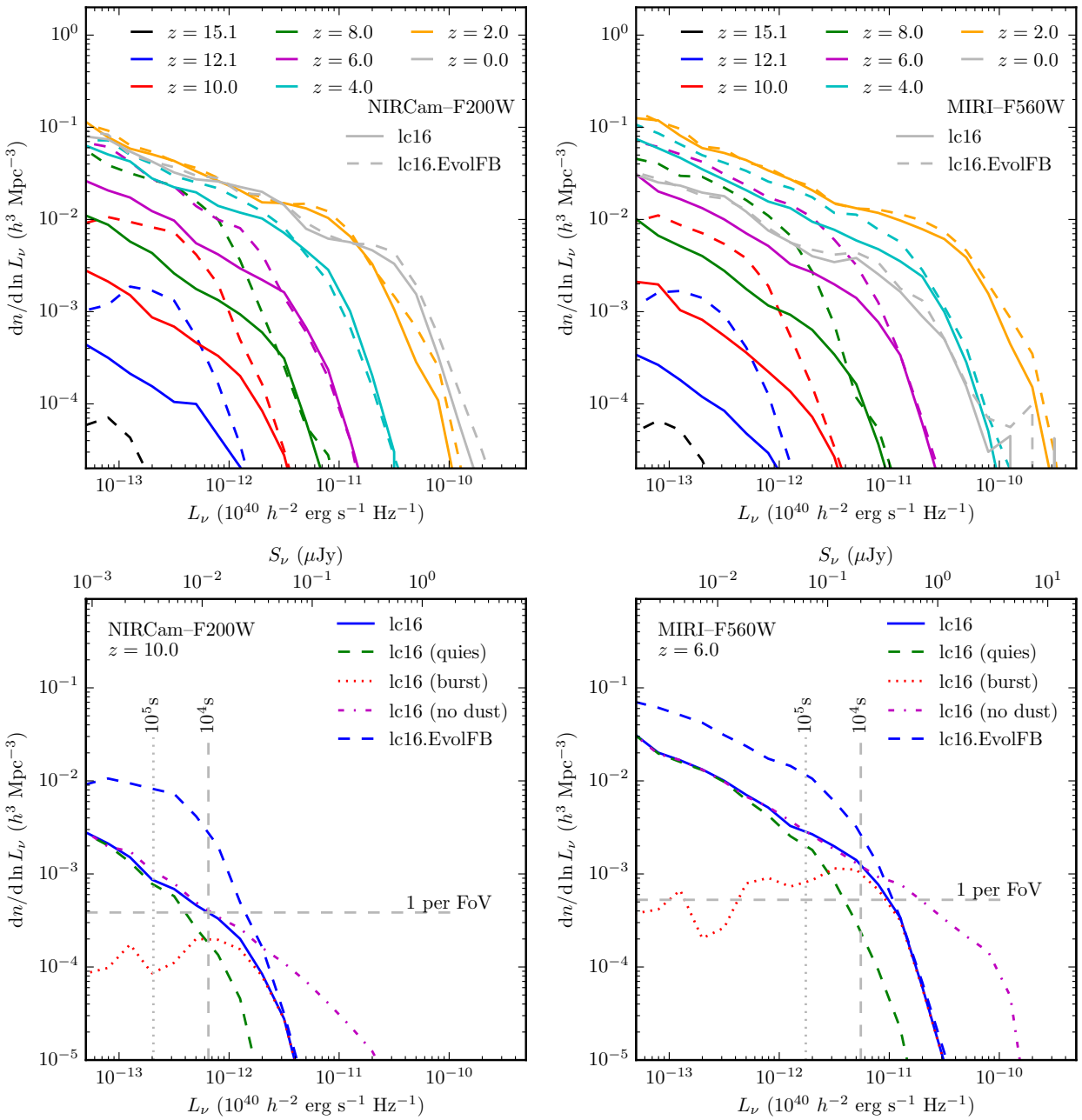

Figure 6. *Top panels*: predicted evolution from $z = 15.1$ to $z = 0.0$ of the luminosity function in the NIRCam–F200W (left panel) and MIRI–F560W (right panel) bands (in the observer-frame). The colour indicates the redshift as shown in the legend. The solid lines show predictions from the fiducial model, whereas the dashed lines show predictions of the evolving feedback variant. *Bottom panels*: a breakdown of the predicted luminosity functions for NIRCam–F200W at $z = 10$ (left panel) and MIRI–F560W at $z = 6$ (right panel). The solid blue lines show the predictions of the fiducial model and the dashed green and dotted red lines show the contribution to this from quiescent and starburst galaxies respectively. The predictions of the fiducial model excluding dust absorption are shown by the dash-dotted magenta lines. The dashed blue line is the prediction from the evolving feedback model. For reference, the horizontal dashed lines indicate the number density at which there is one object per *JWST* field of view at that redshift and the vertical dashed and dotted lines indicate the *JWST* sensitivity limits for that filter for a 10^4 and 10^5 s exposure, as labelled.

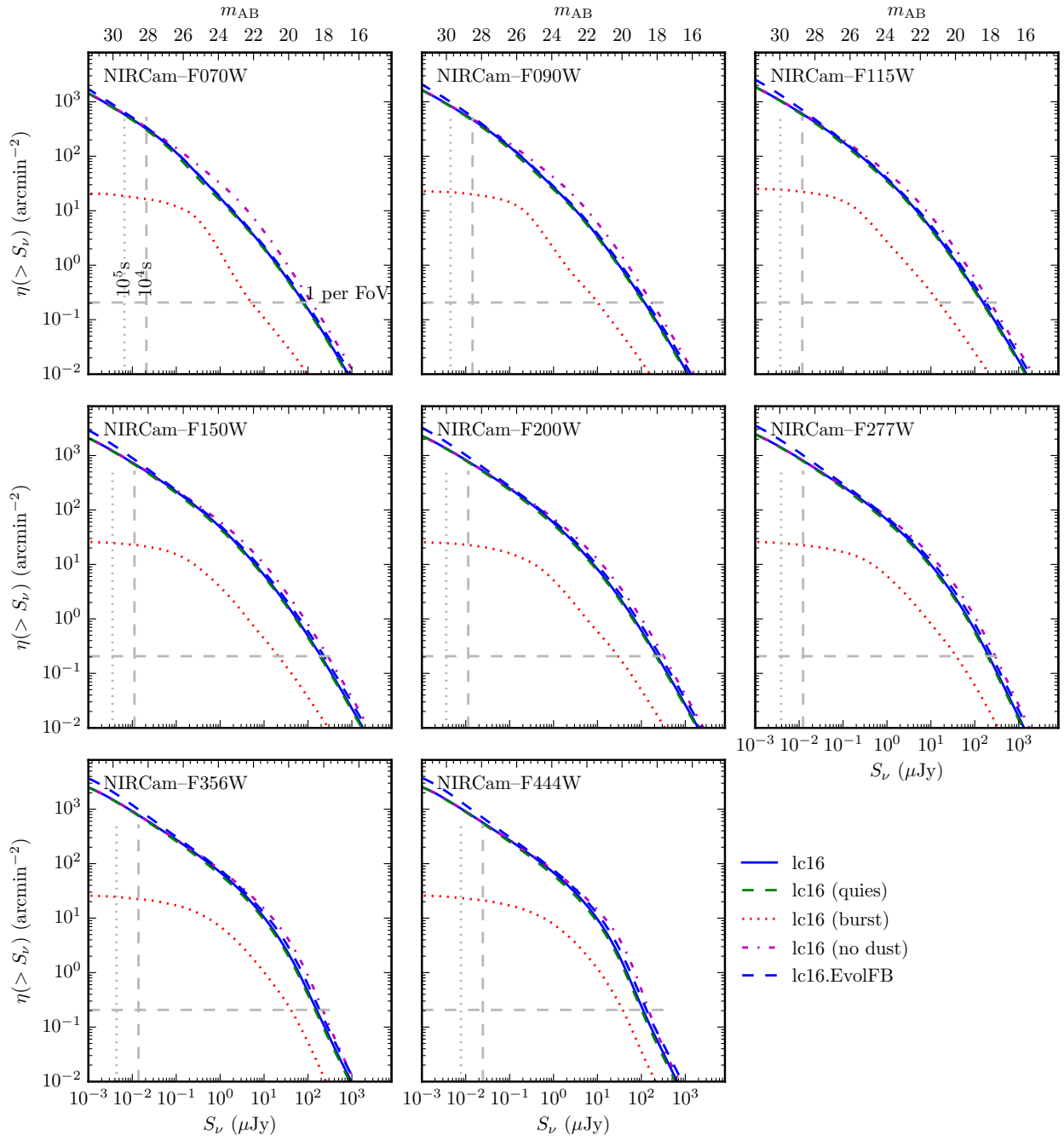

Figure 7. Predicted cumulative galaxy number counts in the NIRCam bands. The name of the band is indicated in each panel. The solid blue lines show the predictions of the fiducial model and the dashed green and dotted red lines show the contribution to this from quiescent and starburst galaxies respectively. The predictions of the fiducial model excluding dust absorption are shown by the dash-dotted magenta lines. The dashed blue lines show the predictions from the evolving feedback variant. For reference, the horizontal dashed lines indicate the number density at which there is one object per field of view and the vertical dashed and dotted lines indicate the sensitivity limits for that filter for a 10^4 and 10^5 s exposure respectively.

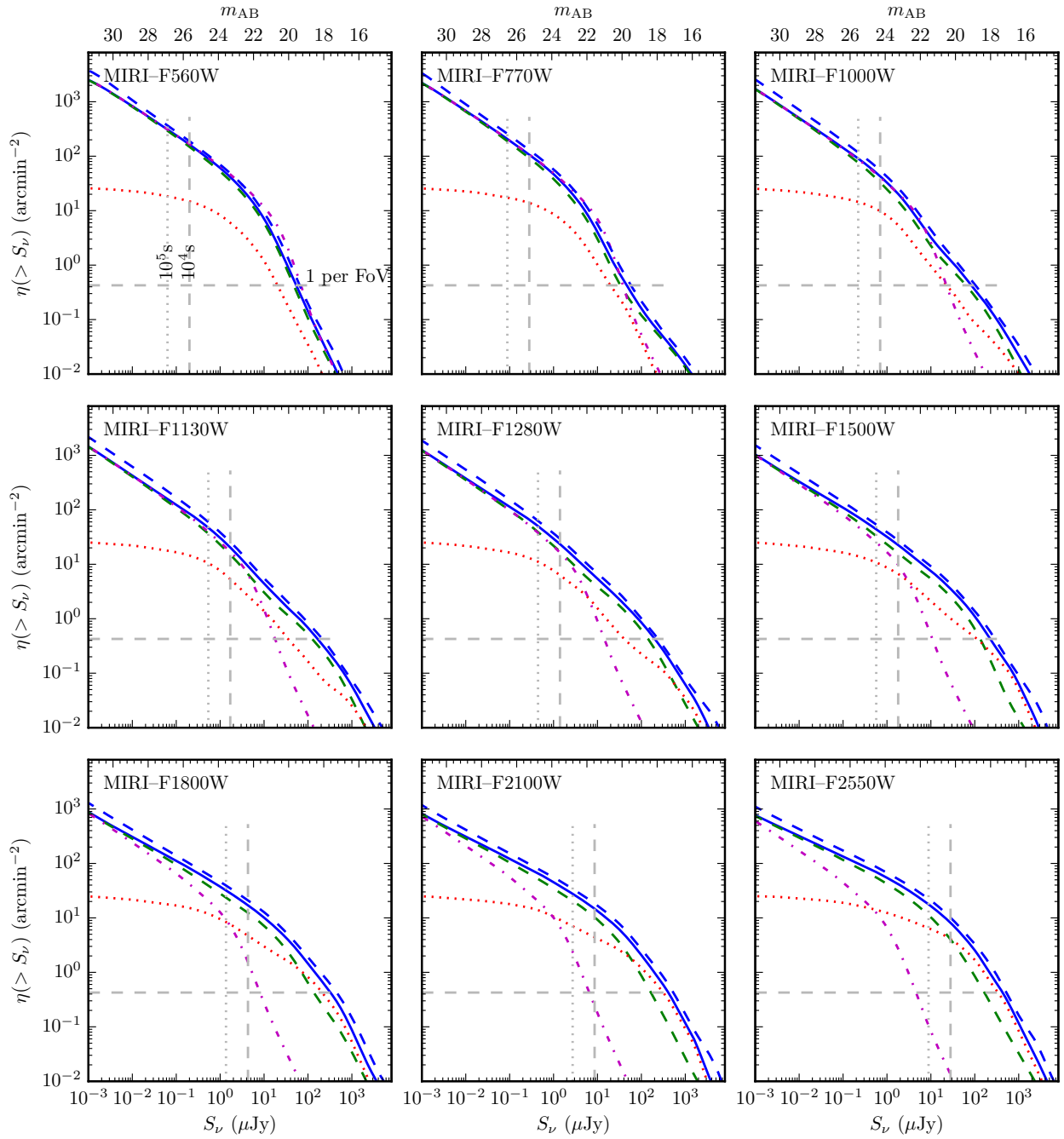

Figure 8. Predicted cumulative galaxy number counts in the MIRI bands. The name of the band is indicated each panel. All lines have the same meaning as in Fig. 7.

servable at $z \gtrsim 10$ with NIRCam and at $z \gtrsim 6$ with MIRI, although we stress that this is the case for a single FoV and a 10^4 s exposure. Additionally, we note that we have not considered effects such as gravitational lensing, which would allow surveys to probe fainter galaxies at higher redshifts (e.g. Infante et al. 2015).

Various features in the predicted MIRI redshift distributions can be related to PAH emission. For example, the peaks at $z \sim 2.5$ in the MIRI–F1130W distribution and at $z \sim 3.6$ in the MIRI-F1500W distribution correspond to the 3.3 μm PAH feature.

We briefly consider the possibility that nebular emission lines may affect our predicted broadband photometry (e.g. Smit et al. 2015), as they are not included in our galaxy SEDs. For this we focus on the MIRI–F560W filter at $z \sim 7$ as the H α emission line is redshifted across the filter. The

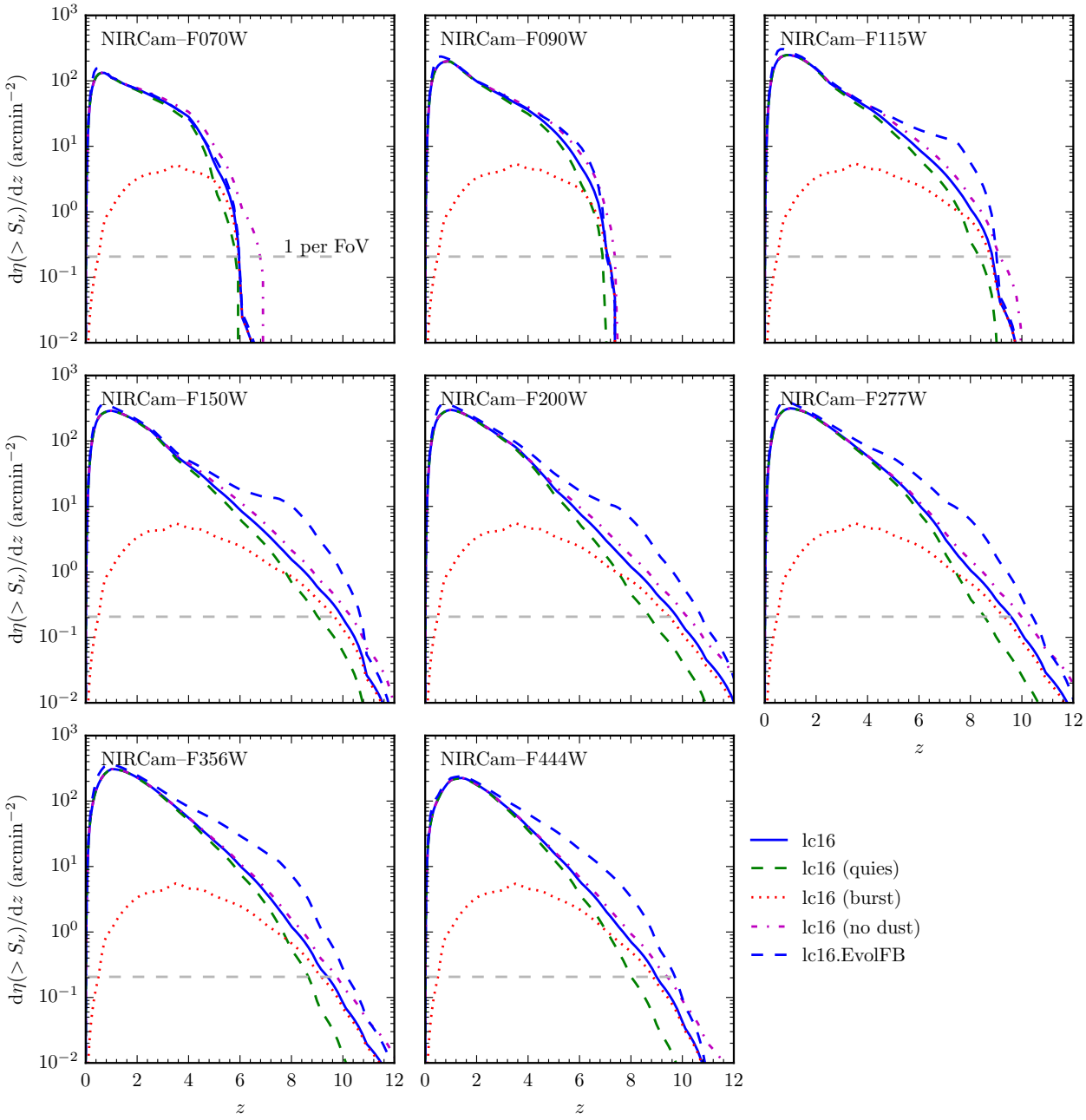

Figure 9. Predicted redshift distributions for objects detectable in a 10^4 s exposure in NIRCam bands. The name of the band is indicated in each panel. The solid blue lines show the predictions of the fiducial model, and the dashed green and dotted red lines show the contribution to this from quiescent and starburst galaxies respectively. The predictions of the fiducial model excluding dust absorption are shown by the dash-dotted magenta lines. The dashed blue lines show the predictions from the evolving feedback variant. For reference, the horizontal dashed line indicates the number density at which there is one object per field of view per unit redshift.

luminosity of the H α line is calculated assuming that all photons emitted with wavelengths shorter than 912 Å will ionize a hydrogen atom in the gas surrounding the star. We then assume 'Case B' recombination i.e. we ignore recombinations directly to the ground state ($n = 1$), as these just produce another ionizing photon. Thus only recombinations to $n > 1$ are counted. The fraction of such recombinations that produce an H α photon ($n = 2 \rightarrow 1$) is taken from Osterbrock (1974). We apply the dust extinction factor predicted by GRASIL at the wavelength of the line to the line

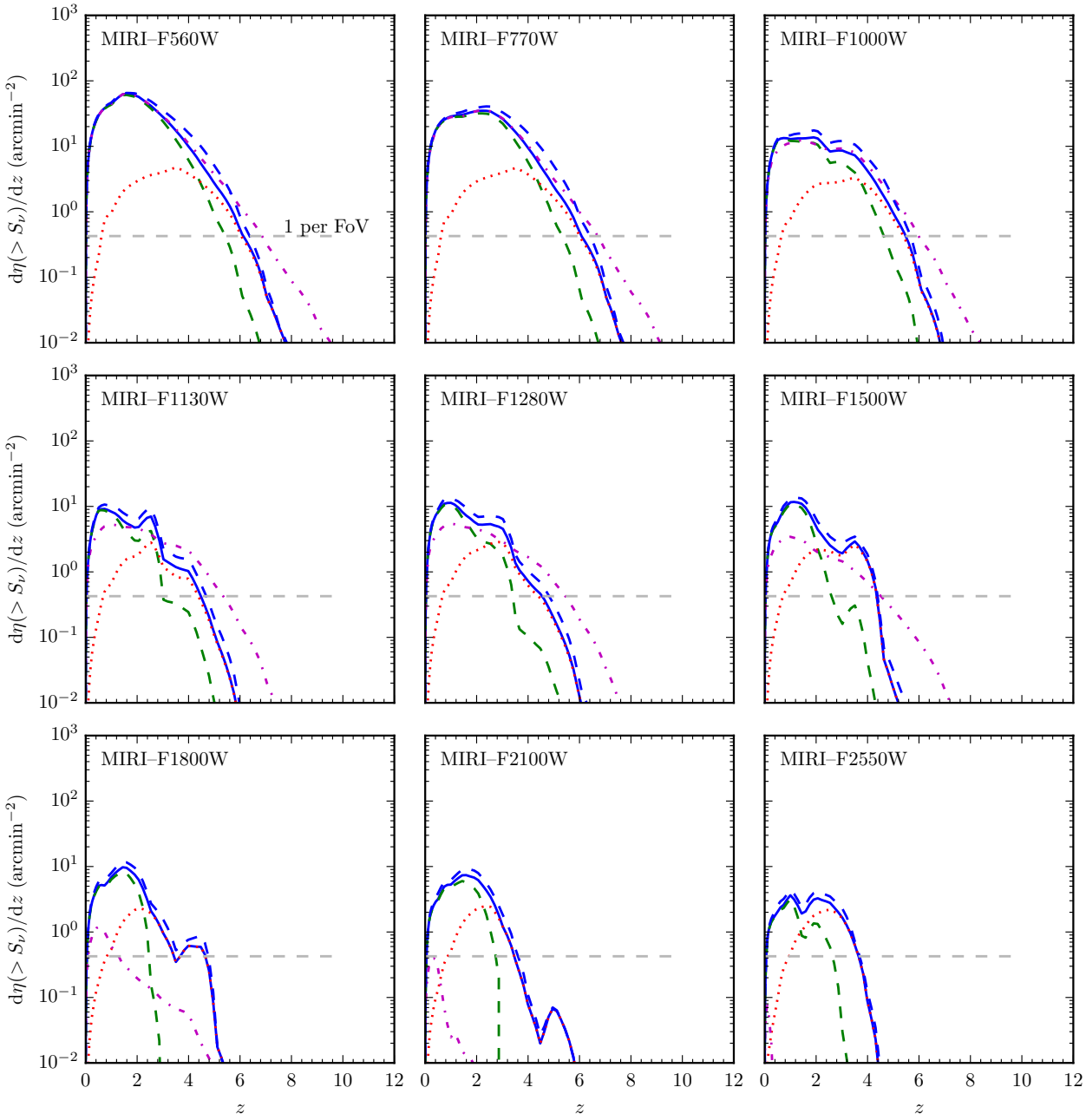

Figure 10. Predicted redshift distributions for galaxies observable with a 10^4 s exposure in MIRI bands. The name of the band is indicated in each panel. All lines have the same meaning as in Fig. 9.

luminosity. We find that the predicted equivalent widths (EWs) of the line are ∼ 400 Å, significantly narrower than the width of the MIRI–F560W filter ∼ 1.2 µm. As a result, the line luminosity has a minor effect on the broadband photometry. For example, at $z = 7.5$ in both models 95 per cent of the sampled galaxies have their MIRI–F560W luminosity increased by less than ∼ 10 per cent, and 90 per cent by less than ∼ 7 per cent. This results in a negligible difference in the luminosity functions if H α emission is included. Thus we conclude that a more detailed inclusion of nebular emission lines (e.g. Panuzzo et al. 2003) is unlikely to affect the results presented here (see also Bisigello et al. 2016 for an investigation of the effect of nebular emission lines on MIRI photometry).

We now consider the predicted redshift distributions of galaxies that would be observable with longer exposures

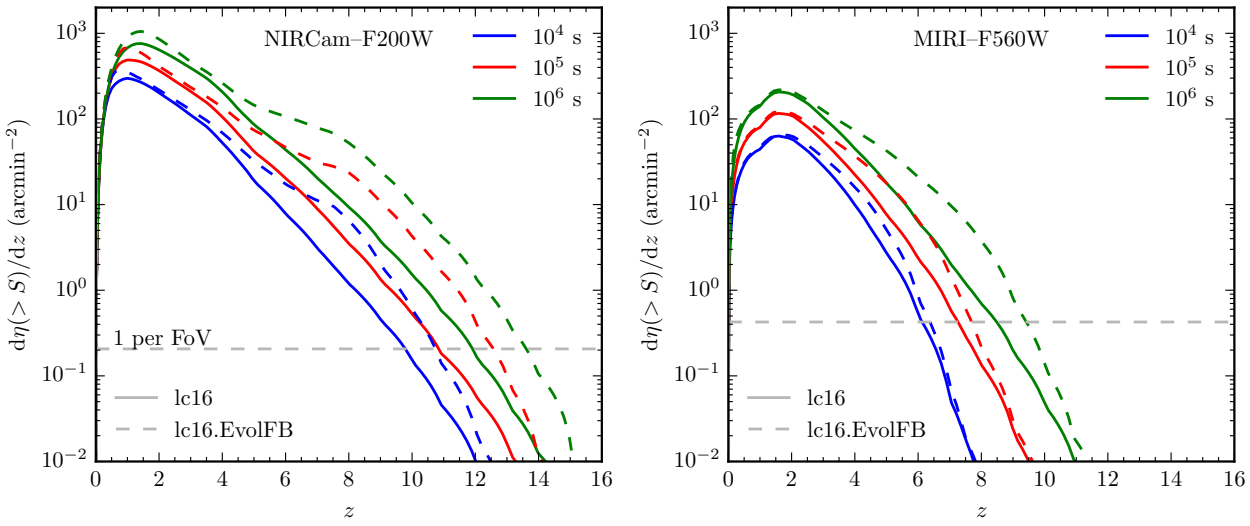

Figure 11. Predicted redshift distributions for the NIRCam–F200W (left panel) and MIRI–F560W (right panel) bands for galaxies observable with a range of exposure times. The blue, red and green lines show predictions for exposures of 10^4, 10^5 and 10^6 s respectively. The solid and dashed lines are the predictions of the fiducial and evolving feedback variant models respectively. For reference, the horizontal dashed lines show the number surface density at which there is one object per field of view per unit redshift.

than considered in Figs 9 and 10. In Fig. 11 we show predictions for 10^4, 10^5 and 10^6 s exposures, for the NIRCam–F200W and MIRI–F560W filters. For the fiducial model a 10^6 s exposure will increase the number of observable objects in the NIRCam–F200W filter at $z \sim 10$ from 1 per FoV to ~ 10 per Fov, and will increase the highest redshift at which an object is observable in a single FoV from $z \sim 10$ to $z \sim 12$. For the evolving feedback model the highest redshift will be $z \sim 14$. Thus, we expect that long ($> 10^4$ s) exposures with *JWST* will provide better constraints on the effectiveness of supernova feedback in galaxies at high redshift.

3.4 Sizes of galaxies in *JWST* bands

Finally, we present predictions for the angular sizes of galaxies for the NIRCam–F200W and MIRI-F560W filters in Fig. 12. We make such preditions for all NIRCam and MIRI filters but show only these two here for brevity, the predictions for other filters will be made available online. The sizes in each band are calculated as described in Section 3.1.

We can see that the predicted sizes are ~ 0.1 arcsec, with the evolving feedback variant generally predicting slightly smaller sizes. By comparison to the diffraction limits for *JWST*, shown here as dashed horizontal lines, it is evident that NIRCam will be able to resolve the majority of detected galaxies whereas this will not be the case for MIRI (for $z \gtrsim 2$).

4 SUMMARY

The *James Webb Space Telescope* (*JWST*) is scheduled for launch in October 2018 and is expected to significantly advance our understanding of the high-redshift ($z \gtrsim 7$) Universe.

Here we present predictions for deep galaxy surveys with *JWST*. To do so we couple the hierarchical galaxy formation model GALFORM (Lacey et al. 2016), with the spectrophotometric code GRASIL (Silva et al. 1998) for computing galaxy SEDs. GRASIL calculates the absorption and re-emission of stellar radiation by interstellar dust by solving the equations of radiative transfer in an assumed geometry. The galaxy formation model is implemented within a dark matter only N-body simulation using *Planck* cosmological parameters (Planck Collaboration et al. 2016). Adjustable parameters in the model are calibrated against a broad range of observational data such as optical and near-IR luminosity functions at $z = 0$, the evolution of the rest-frame near-IR luminosity functions for $z = 0 - 3$, far-IR galaxy number counts and redshift distributions, and the evolution of the rest-frame far-UV luminosity function for $z = 3 - 6$ (Lacey et al. 2016; Baugh et al. in preparation). Here we have shown that the model predicts evolution of the rest-frame far-UV luminosity function for $7 \lesssim z \lesssim 10$, and galaxy sizes for $7 \lesssim z \lesssim 9$, in good agreement with observations.

We also present predictions for an evolving feedback variant model, in which the strength of supernova feedback is allowed to vary as a function of redshift (Hou et al. 2016). This adjustment allows the model to reproduce the reionization redshift inferred from *Planck* data (Planck Collaboration et al. 2016), as well as the luminosity function of the Milky Way satellites and their metallicity–stellar mass relation.

We present predictions for *JWST* in the form of luminosity functions, number counts, redshift distributions and angular sizes for each of the broadband filters on NIRCam and MIRI on *JWST*, for both the fiducial model 'lc16' and the evolving feedback variant 'lc16.EvolFB'.

We find that for a 10^4 s exposure the fiducial model predicts that *JWST* will be able to observe a single galaxy per

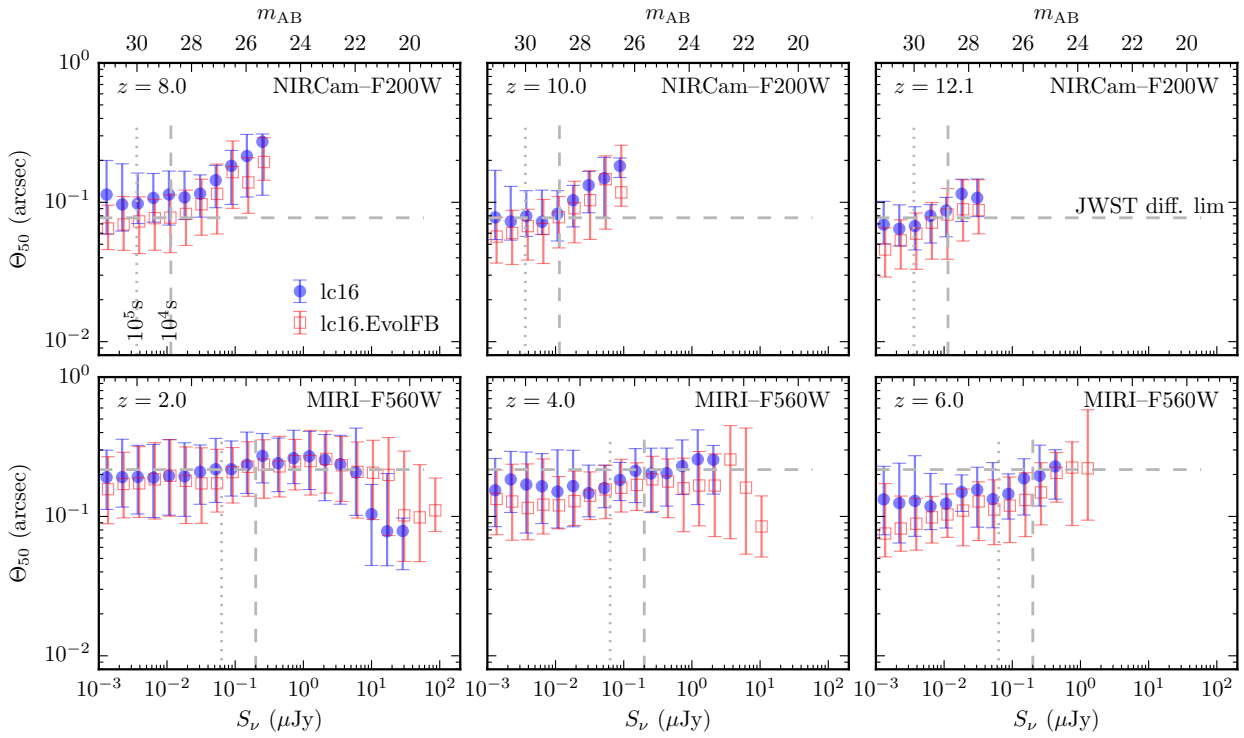

Figure 12. Predicted projected half-light radii at a range of redshifts, as a function of galaxy flux, S_ν. The redshift is indicated in each panel. The top row shows predictions for the NIRCam–F200W filter, the bottom row shows predictions for the MIRI–F560W filter. The blue filled circles and open red squares respectively indicate the median size for the fiducial and evolving feedback variant models at a given flux, with the errorbars indicating the 16-84 percentile ranges in a given flux bin. For reference, the vertical dashed and dotted lines respectively indicate the sensitivity limit for a 10^4 and 10^5 s exposure for that filter. The horizontal dashed line indicates the diffraction limit of *JWST* for that filter, assuming a 6.5 m diameter mirror.

field of view at $z \sim 10$ in the NIRCam–F200W filter; though the evolving feedback model predicts number surface densities factors of ~ 5 greater. The model predicts that similar exposures with MIRI will not detect any galaxies at $z \gtrsim 6$ (in a single FoV). Longer integration times will increase the number of galaxies that are observable, for example, a 10^6 s integration will increase the number of galaxies predicted by the fiducial model to be observable in a single FoV by a factor of ~ 10. A similar effect may be achieved by utilising strong gravitational lenses; however, we do not consider such an effect here. We consider a simple model for calculating H α emission and conclude that nebular emission lines will have a negligible effect on these results.

The predicted sizes of high-redshift galaxies observable with *JWST* are ~ 0.1 arcsec, and as such we expect NIRCam to be capable of resolving the majority of detected galaxies.

We hope that the predictions presented here will help inform galaxy survey strategies for *JWST*. In the future we plan to make our results public for such a purpose, and to further develop our methodology to produce realistic mock galaxy catalogues for NIRCam and MIRI. This will allow us to make direct predictions for field-to-field variance. We envisage that observations with *JWST* will provide a wealth of information on physical processes important for galaxy formation, such as the effectiveness of supernova feedback in galaxies at high redshift.

ACKNOWLEDGEMENTS

The authors would like to thank Alessandro Bressan, Gian-Luigi Granato and Laura Silva for use of, and discussions relating to, the GRASIL code. Additionally, we would like to acknowledge Karina Caputi, Lydia Heck, John Helly, Hou Jun, Sarah Kendrew, John Pye, Luiz Felippe Rodrigues, Martin Ward and Rogier Windhorst for many helpful discussions during the development of this work. This work was supported by the Science and Technology Facilities Council [ST/K501979/1, ST/L00075X/1]. CMB acknowledges the receipt of a Leverhulme Trust Research Fellowship. CSF acknowledges an ERC Advanced Investigator Grant, COSMIWAY [GA 267291] and the Science and Technology Facilities Council [ST/F001166/1, ST/I00162X/1]. This work used the DiRAC Data Centric system at Durham University, operated by the Institute for Computational Cosmology on behalf of the STFC DiRAC HPC Facility (www.dirac.ac.uk). This equipment was funded by BIS National E-infrastructure capital grant ST/K00042X/1, STFC capital grant ST/H008519/1, and STFC DiRAC Operations grant ST/K003267/1 and Durham University. DiRAC is part of the National E-Infrastructure.

References

Agladze N. I., Sievers A. J., Jones S. A., Burlitch J. M., Beckwith S. V. W., 1996, ApJ, 462, 1026

Almeida C., Baugh C. M., Lacey C. G., Frenk C. S., Granato G. L., Silva L., Bressan A., 2010, MNRAS, 402, 544
Baugh C. M., Cole S., Frenk C. S., Lacey C. G., 1998, ApJ, 498, 504
Baugh C. M., Lacey C. G., Frenk C. S., et al. 2005, MNRAS, 356, 1191
Bisigello L., et al., 2016, ApJS, 227, 19
Bouwens R. J., et al., 2003, ApJ, 595, 589
Bouwens R. J., et al., 2010, ApJ, 709, L133
Bouwens R. J., et al., 2015, ApJ, 803, 34
Bowler R. A. A., et al., 2014, MNRAS, 440, 2810
Caputi K. I., Cirasuolo M., Dunlop J. S., McLure R. J., Farrah D., Almaini O., 2011, MNRAS, 413, 162
Caputi K. I., et al., 2015, ApJ, 810, 73
Cole S., 1991, ApJ, 367, 45
Cole S., Aragon-Salamanca A., Frenk C. S., Navarro J. F., Zepf S. E., 1994, MNRAS, 271, 781
Cole S., Lacey C. G., Baugh C. M., Frenk C. S., 2000, MNRAS, 319, 168
Cowley W. I., Bethermin M., Lagos C. d. P., Lacey C. G., Baugh C. M., Cole S., 2016, preprint, (arXiv:1607.05717)
Draine B. T., Lee H. M., 1984, ApJ, 285, 89
Finkelstein S. L., et al., 2015, ApJ, 810, 71
Gardner J. P., et al., 2006, Space Sci. Rev., 123, 485
Granato G. L., Lacey C. G., Silva L., et al. 2000, ApJ, 542, 710
Guo Q., White S., Angulo R. E., et al. 2013, MNRAS, 428, 1351
Helly J. C., Cole S., Frenk C. S., et al. 2003, MNRAS, 338, 903
Hou J., Frenk C. S., Lacey C. G., Bose S., 2016, MNRAS,
Infante L., et al., 2015, ApJ, 815, 18
Jiang C. Y., Jing Y. P., Faltenbacher A., Lin W. P., Li C., 2008, ApJ, 675, 1095
Jiang L., Helly J. C., Cole S., Frenk C. S., 2014, MNRAS, 440, 2115
Komatsu E., Smith K. M., Dunkley J., et al. 2011, ApJS, 192, 18
Labbé I., et al., 2005, ApJ, 624, L81
Lacey C. G., Baugh C. M., Frenk C. S., Silva L., Granato G. L., Bressan A., 2008, MNRAS, 385, 1155
Lacey C. G., Baugh C. M., Frenk C. S., Benson A. J., 2011, MNRAS, 412, 1828
Lacey C. G., et al., 2016, MNRAS, 462, 3854
Lagos C. d. P., Lacey C. G., Baugh C. M., 2013, MNRAS, 436, 1787
Larson R. B., 1974, MNRAS, 169, 229
Lewis A., 2008, Phys. Rev. D, 78, 023002
Maraston C., 2005, MNRAS, 362, 799
Meiksin A., 2005, MNRAS, 356, 596
Mitchell P. D., Lacey C. G., Cole S., Baugh C. M., 2014, MNRAS, 444, 2637
Mo H. J., Fukugita M., 1996, ApJ, 467, L9
Mo H. J., Mao S., White S. D. M., 1999, MNRAS, 304, 175
Oesch P. A., et al., 2014, ApJ, 786, 108
Oke J. B., 1974, ApJS, 27, 21
Ono Y., et al., 2013, ApJ, 777, 155
Osterbrock D. E., 1974, Astrophysics of gaseous nebulae
Panuzzo P., Bressan A., Granato G. L., Silva L., Danese L., 2003, A&A, 409, 99
Peng C. Y., Ho L. C., Impey C. D., Rix H.-W., 2002, AJ, 124, 266
Planck Collaboration et al., 2016, A&A, 594, A13
Sawala T., Frenk C. S., Crain R. A., Jenkins A., Schaye J., Theuns T., Zavala J., 2013, MNRAS, 431, 1366
Schaye J., et al., 2015, MNRAS, 446, 521
Schenker M. A., et al., 2013, ApJ, 768, 196
Shibuya T., Ouchi M., Harikane Y., 2015, ApJS, 219, 15
Silva L., Granato G. L., Bressan A., Danese L., 1998, ApJ, 509, 103
Simha V., Cole S., 2016, preprint, (arXiv:1609.09520)
Smit R., et al., 2015, ApJ, 801, 122
Springel V., White S. D. M., Jenkins A., et al. 2005, Nature, 435, 629
Stanway E. R., Bunker A. J., McMahon R. G., 2003, MNRAS, 342, 439
Steidel C. C., Hamilton D., 1993, AJ, 105, 2017
Steidel C. C., Giavalisco M., Pettini M., Dickinson M., Adelberger K. L., 1996, ApJ, 462, L17
Swinbank A. M., Lacey C. G., Smail I., et al. 2008, MNRAS, 391, 420
Vogelsberger M., et al., 2014, MNRAS, 444, 1518
White S. D. M., Frenk C. S., 1991, ApJ, 379, 52
White S. D. M., Rees M. J., 1978, MNRAS, 183, 341
Wilkins S. M., Bunker A. J., Ellis R. S., Stark D., Stanway E. R., Chiu K., Lorenzoni S., Jarvis M. J., 2010, MNRAS, 403, 938

This paper has been typeset from a TEX/LATEX file prepared by the author.